Exp.-Nr. **A2**

Eingang:

an PAC:

Mainz Microtron MAMI

A2 Collaboration at MAMI

Spokespersons: P. Pedroni, A. Thomas

Proposal for an Experiment

"Photoproduction of Kaons off the Neutron"

Spokespersons for the Experiment :

Natalie K. Walford (University of Basel, Switzerland)

Abstract of Physics :

It is proposed to measure kaon photoproduction from neutrons using a liquid deuterium target and deuterated butanol target. The production thresholds for $K^0\Lambda$, $K^0\Sigma^0$, and $K^+\Sigma^-$ are $\approx$ 916 MeV, 1049 MeV, and 1051 MeV, respectively. While previous studies in kaon photoproduction focused on low-lying baryon resonances, most states above 1350 MeV have not been observed, despite their expected existence based on theoretical models. Polarization observables provide important information, in particular in the non-pertubative regime of QCD. Therefore, the measurement of polarization observables and unpolarized cross section measurements is proposed, specifically targeted at photon energies above 1350 MeV. For MAMI, the aim is to measure the beam-target observables E, T, and F, and the recoil observables T_x, T_z, L_x, and L_z using the deuterated butanol target, as well as $\frac{d\sigma}{d\Omega}$, C_x, and C_z using liquid deuterium, both together with a circularly polarized photon beam for $K^+\Sigma^-$.

Abstract of Equipment :

The experiment will be performed at the tagged photon facility of MAMI (Glasgow Tagger) using the Crystal Ball/TAPS detector setup together with the particle identification detector (PID) and multi-wire proportional chambers (MWPCs).

MAMI Specifications :

beam energy	1604 MeV
beam current	< 100 nA
beam polarization	polarized

Photon Beam Specifications :

tagged energy range	1550 MeV (endpoint tagger)
photon beam polarization	circularly polarized photons

Equipment Specifications :

detectors	Crystal Ball/TAPS, PID, MWPCs
target	liquid deuterium and polarized deuterated butanol

Beam Time Request :

set-up/test with beam	24 hours
DATA Taking	$\approx$ 200 hours with deuterium target
	$\approx$ 500 hours with D-Butanol
	$\approx$ 100 hours with carbon target for background subtraction

List of participating authors:

- **Institut für Physik, University of Basel, Switzerland**
  S. Abt, S. Garni, M. Günther, A. Käser, B. Krusche, S. Lutterer, M. Oberle, Th. Strub, N.K. Walford, L. Witthauer
- **Institut für Experimentalphysik, University of Bochum, Germany**
  G. Reicherz
- **Helmholtz–Institut für Strahlen- und Kernphysik, University of Bonn, Germany**
  F. Afzal, R. Beck, K. Spieker, A. Thiel
- **JINR, Dubna, Russia**
  N.S. Borisov, A. Lazarev, A. Neganov, Yu.A. Usov
- **SUPA School of Physics, University of Edinburgh, UK**
  M. Bashkanov, S. Kay, D.P. Watts, L. Zana
- **SUPA School of Physics and Astronomy, University of Glasgow, UK**
  J.R.M. Annand, S. Gardner, D.I. Glazier, D. Hamilton, K. Livingston, R. Macrae, I.J.D. MacGregor, C. Mullen, D. Werthmüller
- **Department of Astronomy and Physics, Saint Mary's University Halifax, Canada**
  A.J. Sarty
- **Racah Institute of Physics, Hebrew University of Jerusalem, Israel**
  G. Ron
- **Kent State University, Kent, USA**
  C.S. Akondi, D.M. Manley
- **Institut für Kernphysik, University of Mainz, Germany**
  P. Achenbach, H.J. Arends, M. Biroth, F. Cividini, A. Denig, P. Drexler, M.I. Ferretti-Bondy, W. Gradl, V.L Kashevarov, P.P. Martel, A. Neiser, E. Mornacchi, M. Ostrick, S.N. Prakhov, V. Sokhoyan, C. Sfienti, O. Steffen, M. Thiel, A. Thomas, S. Wagner, J. Wettig, M. Wolfes
- **University of Massachusetts, Amherst, USA**
  R.Miskimen, A. Rajabi
- **Institute for Nuclear Research, Moscow, Russia**
  G. Gurevic, R. Kondratiev, V. Lisin, A. Polonski

- **INFN Sezione di Pavia, Pavia, Italy**

  A. Braghieri, S. Costanza, P. Pedroni

- **Department of Physics, University of Regina, Canada**

  Z. Ahmed, G.M. Huber, D. Paudyal

- **Mount Allison University, Sackville, Canada**

  D. Hornidge

- **Tomsk Polytechnic University, Tomsk, Russia**

  A. Fix

- **George Washington University, Washington, USA**

  W.J. Briscoe, C. Collicott, E.J. Downie, I.I. Strakovski

- **Rudjer Boskovic Institute, Zagreb, Croatia**

  M. Korolija, I. Supek

1 Introduction

A large effort in recent years has been done by labs such as MAMI, Jefferson Lab, and CB-ELSA for the search for undiscovered states of the nucleon. In order to provide the data batase with nearly model-independent partial wave analyses (PWA), the search for such states must be probed. Polarization observables are essential for disentangling the contributing resonant and non-resonant amplitudes of the states. The motivation for the study of kaon photoproduction off the neutron will be discussed and the benefits that can deduced from it.

1.1 Motivation

In order to understand the underlying interactions of the excitation spectrum of the nucleon, Quantum Chromodynamics (QCD) must be fully explored. Specifically, a complete depiction of the spectrum of N^* and Δ^* resonances is essential to understanding the excitation spectrum. Currently, a major challenge in hadronic physics is attempting to understand the nonperturbative nature of QCD at low energies. Phenomenological models are the current leading tool used for this task. The models have represented the internal structure of the nucleon as three constituent valence quarks that interact with each other and focus on identifying the effective degrees of freedom. The SU(6)$\times$(3) symmetry is used by quark models in order to predict the number of nucleon resonances. However, the quark models predict many states that are currently missing from the baryon spectrum. One of the main rationales for the reason why the states are missing is because the resonances couple weakly to the πN channel.

πN scattering was once the leading tool used to discover baryon states. The lowest energy quark model state in each oscillator band couples strongly to πN, while the πN coupling strengths tend to decrease rapidly as the masses of the states increase [1]. In recent years, the effort to study the photoproduction of pseudo scalar mesons has increased. It is hope that the study of decay channels such as $\pi\pi N$, ρN, ωN, ηN, $K\Lambda$, and $K\Sigma$ will reveal new states [2] [3]. However, kaon photoproduction has much smaller cross sections than π production and data from the neutron is almost nonexistent.

Due to the lack of constraining data, the fluctuations in the predicted $\gamma n \rightarrow KY$ cross sections are sizable. The fluctuations are caused from several problems in the PWA. Most resonances are extremely broad and overlapping and have decay branches to many final states. Also, the presence of a s-channel resonance assures contributions from the corresponding u-channel processes, which are non-resonant, and contribute to large number of partial waves and

interfere with other resonances. Furthermore, it has been well-established that cross section data alone is not enough to define the amplitudes of meson-production and polarization observables are required to avoid ambiguities [4]. Polarization observables are useful as they are composed of ratios of cross sections and systematics related to flux normalization and detector acceptance mostly cancel.

Hyperon photoproduction can be described by four complex amplitudes, which stems from the the two photon-spin states and the two nucleon-spin states, and leads to a total of sixteen experimental observables. By summing the squares of the amplitudes, the differential cross section can be calculated. The sixteen observables can be seen in Table 1 and are divided into groups based on the beam polarization, target polarization, or recoil hyperon polarization. This proposal will most focus on the observables obtained using a polarized target and circularly polarized photons.

Table 1: The 16 spin observables for $\gamma n \to K^+\Sigma^-$ expressed in the transversity representation. The set label $\mathcal{S}$ refers to single polarization observables, $\mathcal{BT}$ refers to beam-target observables, $\mathcal{BR}$ refers to beam-recoil observables, and $\mathcal{TR}$ refers to target-recoil observables. Polarization of the photon beam is denoted as l for a linearly polarized beam and c for a circularly polarized beam. This table is compiled from Refs. [4] [5].

Spin	Polarization			Transversity	Set
Observable	Beam	Target	Recoil	Representation	
$\left(\frac{d\sigma}{d\Omega}\right)_u$	-	-	-	$\frac{1}{2}(\lvert b_1\rvert^2 + \lvert b_2\rvert^2 + \lvert b_3\rvert^2 + \lvert b_4\rvert^2)$	
Σ	l	-	-	$\frac{1}{2}(\lvert b_1\rvert^2 + \lvert b_2\rvert^2 - \lvert b_3\rvert^2 - \lvert b_4\rvert^2)$	$\mathcal{S}$
T	-	y	-	$\frac{1}{2}(\lvert b_1\rvert^2 - \lvert b_2\rvert^2 - \lvert b_3\rvert^2 + \lvert b_4\rvert^2)$	
P	-	-	y'	$\frac{1}{2}(\lvert b_2\rvert^2 + \lvert b_4\rvert^2 - \lvert b_1\rvert^2 - \lvert b_3\rvert^2)$	
E	c	z	-	$\mathrm{Re}(b_1 b_3^* + b_2 b_4^*)$	
F	c	x	-	$\mathrm{Im}(b_1 b_3^* - b_2 b_4^*)$	$\mathcal{BT}$
G	l	z	-	$\mathrm{Im}(-b_1 b_3^* - b_2 b_4^*)$	
H	l	x	-	$\mathrm{Re}(b_1 b_3^* - b_2 b_4^*)$	
O_x	l	-	x'	$\mathrm{Re}(-b_1 b_4^* + b_2 b_3^*)$	
O_z	l	-	z'	$\mathrm{Im}(b_1 b_4^* + b_2 b_3^*)$	$\mathcal{BR}$
C_x	c	-	x'	$\mathrm{Im}(b_2 b_3^* - b_1 b_4^*)$	
C_z	c	-	z'	$\mathrm{Re}(-b_1 b_4^* - b_2 b_3^*)$	
T_x	-	x	z'	$\mathrm{Re}(b_1 b_2^* - b_3 b_4^*)$	
T_z	-	x	z'	$\mathrm{Im}(b_3 b_4^* - b_1 b_2^*)$	$\mathcal{TR}$
L_x	-	z	x'	$\mathrm{Im}(-b_1 b_2^* - b_3 b_4^*)$	
L_z	-	z	z'	$\mathrm{Re}(-b_1 b_2^* - b_3 b_4^*)$	

The main reaction of interest for this proposal is $\gamma n \to K^+\Sigma^-$. Some properties of the particles that will be detected are shown in Table 2. This reaction is of desirable interest because few polarization observables have been measured, only the differential cross section $\frac{d\sigma}{d\Omega}$ and the beam asymmetry Σ, which are discussed in Sec. 1.3. Due to simple isospin rules, N^* resonances couple strongly to $K^0\Sigma^+$ and $K^+\Sigma^-$ channels. Δ^* resonances couple strongly to $K^+\Sigma^0$ and $K^0\Sigma^0$ channels, so a comparison between $K^+\Sigma^-$ and $K^+\Sigma^0$ is an important tool to allow for identifying contributions from N^* and Δ^* resonances.

Table 2: Properties of the particles detected in this proposal. Compiled from [6].

	K^+	Σ^-
mass (MeV)	493.677	1197.449
isospin	$\frac{1}{2}$	1
quark composition	$u\bar{s}$	dds
spin	0	$\frac{1}{2}$
mean life τ (s)	1.238×10^{-8}	1.479×10^{-10}
main decay channels	$\mu^+\nu_\mu$ (63.4%)	$n\pi^-$ (99.85%)
	$\pi^+\pi^0$ (21.1%)	

Fig. 1 shows the dominant graphs in KY production on the neutron according to Laget [7]. Laget's model estimates the thresholds for certain effects on hyperon photoproduction from the deuteron. In graph (I), the production of KY on the neutron is mediated via t-channel exchange of K or K^*. The rescattering contributions, depicted in graph (II) for the hyperonnucleon and in graph (III) for the kaon-nucleon rescattering vertex, dominate at high proton momenta. The contributions for both rescattering processes are maximal for on-shell propagators in the loop, i.e. when the spectator momentum in the loop vanishes; or in other words, when both nucleons in the deuteron are at rest and the hyperon or kaon is produced on one nucleon and rescatters off the other nucleon, which then obtains its recoil momentum p_1. In this model, the rescattering amplitudes only depend on low-momentum components of the deuteron wave function and on-shell matrix elements, and thus can be calculated readily. Laget has shown that the contributions of graphs (II) and (III) are quite small for small spectator momenta p_1, with $p_1 \leq 0.2$ GeV; there, quasifree production, with the proton as a spectator, dominates.

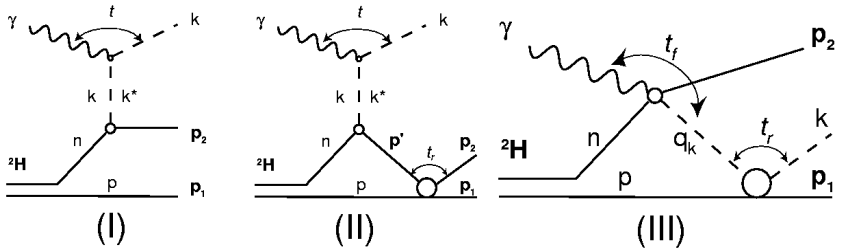

Figure 1: Dominant graphs in KY production on the neutron according to Laget's model [7]: proton as spectator particle (I), hyperon rescattering (II), kaon rescattering (III). k is the outgoing kaon momentum and p_1, and p_2 are the outgoing baryon momenta.

1.2 Theoretical Models

As previously mentioned, QCD cannot fully calculate baryons and their excited states, and models are used to describe the data and predict transition amplitudes and observables in kinematic regions that have not yet been measured. Instead of using fundamental quark and gluon degrees of freedom, hadronic degrees of freedom are used instead. Numerous models are available, but the most relevant to this proposal are from KAON-MAID [8] and the Regge-3 Model [10].

1.2.1 KAON-MAID Model

Maintained by the Institut für Kernphysik at the University of Mainz of Mainz, Germany, KAON-MAID is a theoretical calculative model [8]. KAON-MAID is an isobar model with final-state interactions and presents a tree-level model of kaon photoproduction that includes hadronic form factors at the vertices with gauge invariance using SU(3) values for the Born couplings, non-resonant propagators, and a set of resonances that are consistent with previous analyses. The website of KAON-MAID provides model predictions for not only the differential cross section, but for all polarization observables. KAON-MAID is attempting to find the kinematic range of distortion effects, which also allows one to establish the sensitivity of polarization observables to the elementary amplitude, but are not affected by relativistic effects or particular nuclear targets. Some of their results can be seen in Figs. 2-5, although the model has not been updated in many years. Also shown in Fig. 7 is the angular distribution calculations that are influenced by helicity photon couplings.

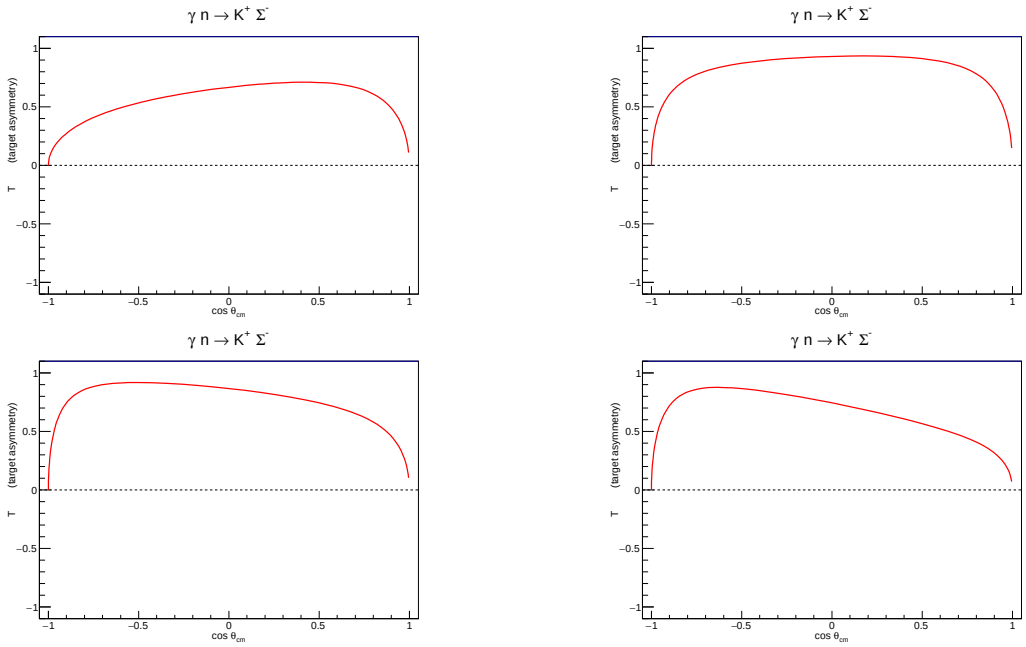

Figure 2: T asymmetry calculations by KAON-MAID in 50 MeV bins. Upper left is 1700 MeV, upper right is 1750 MeV, lower left is 1800 MeV, and bottom right is 1850 MeV.

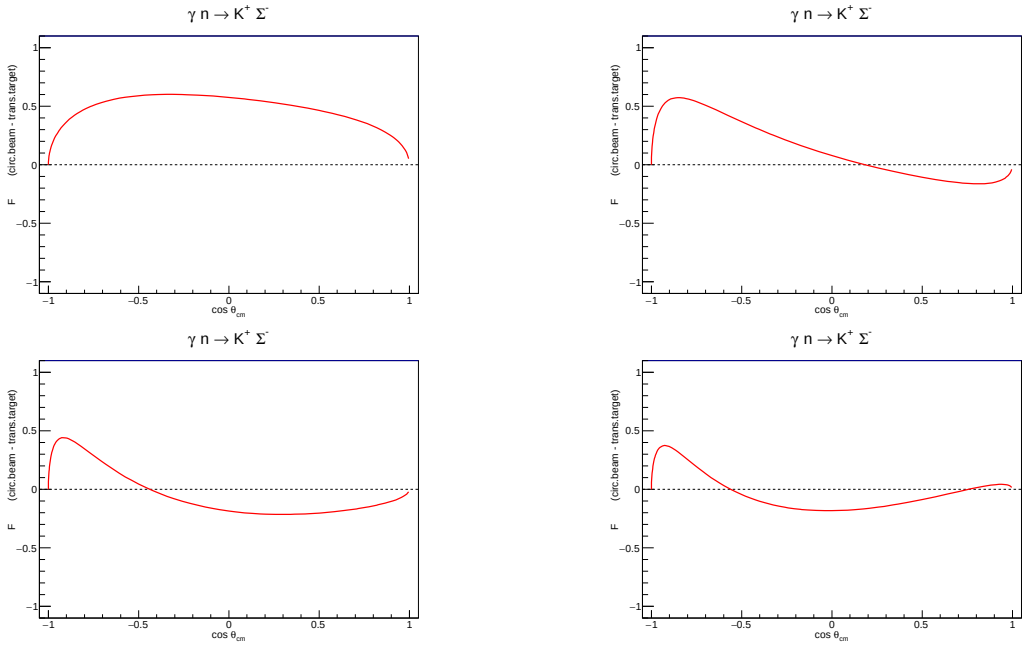

Figure 3: F asymmetry calculations by KAON-MAID in 50 MeV bins. Upper left is 1700 MeV, upper right is 1750 MeV, lower left is 1800 MeV, and bottom right is 1850 MeV.

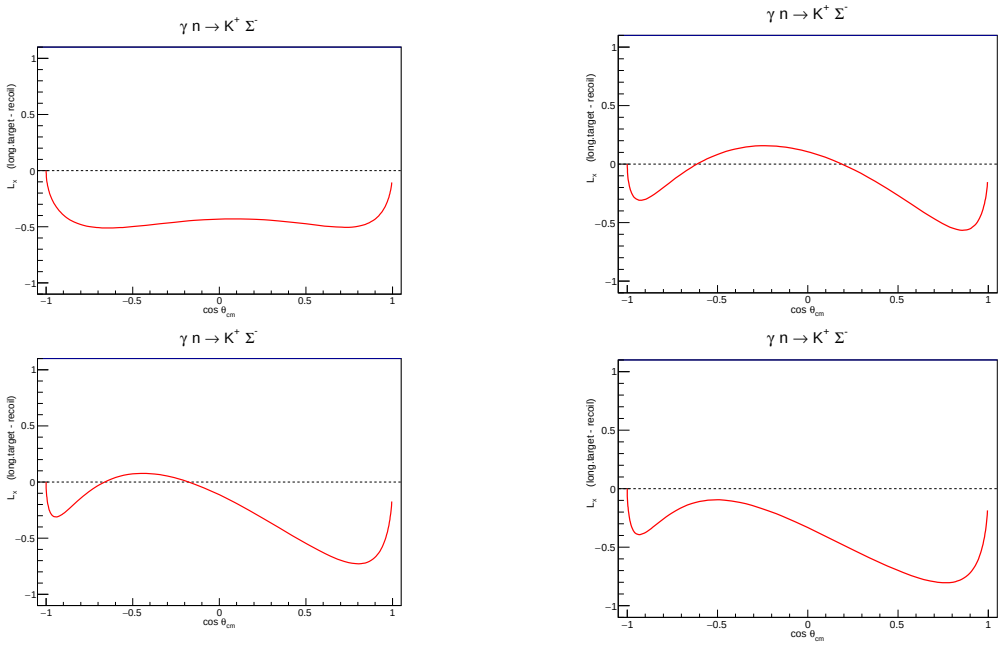

Figure 4: L_x asymmetry calculations by KAON-MAID in 50 MeV bins. Upper left is 1700 MeV, upper right is 1750 MeV, lower left is 1800 MeV, and bottom right is 1850 MeV.

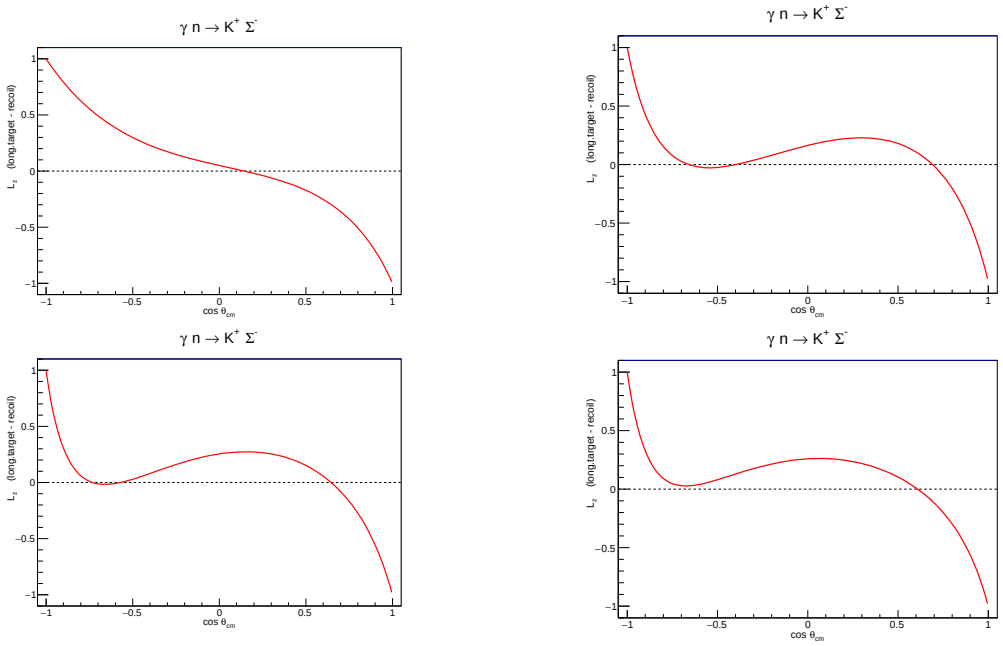

Figure 5: L_z asymmetry calculations by KAON-MAID in 50 MeV bins. Upper left is 1700 MeV, upper right is 1750 MeV, lower left is 1800 MeV, and bottom right is 1850 MeV.

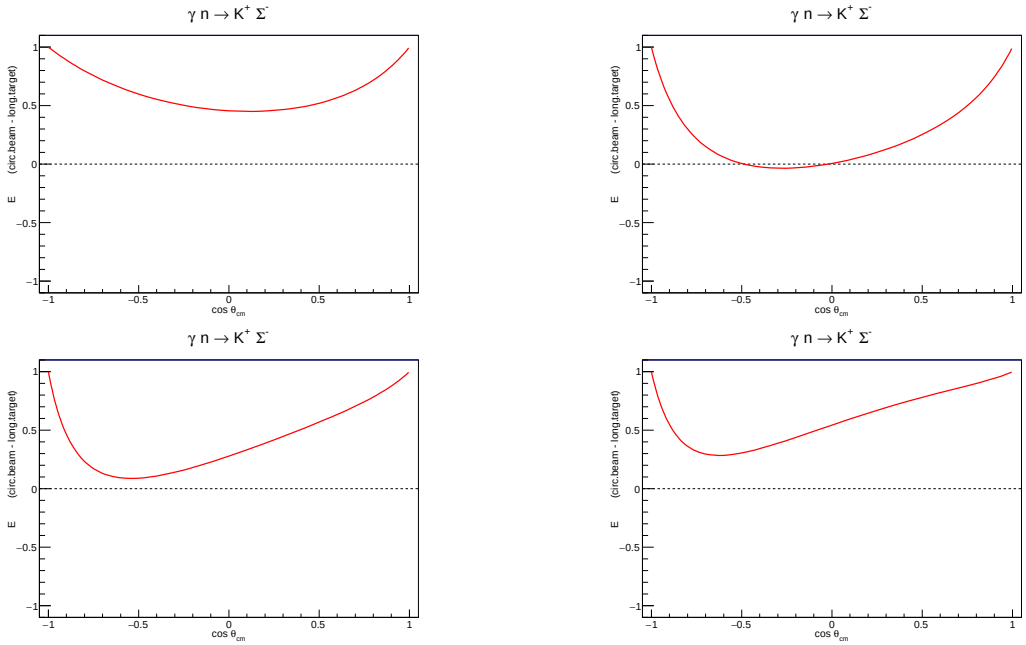

Figure 6: E asymmetry calculations by KAON-MAID in 50 MeV bins. Upper left is 1700 MeV, upper right is 1750 MeV, lower left is 1800 MeV, and bottom right is 1850 MeV.

1.2.2 Regge Model

The Regge Model is a model for high energy pion and kaon photoproduction, which interpolates between the low and higher momentum transfer regions. The model allows for an economical description of unpolarized and polarized data for kaon photoproduction at low momentum transfer. Here, the normalization of the amplitudes are given by the coupling constants at the vertices of the Fenyman diagrams. It is also noted that with the lack of experimental constraints and the approximations of the isobaric models for kaon photoproduction, an alternative way to estimate the coupling constants is to use SU(3) symmetry. [12] Different Regge model predictions can be seen in Fig. 9 and 10. Fig. 9 includes experimental data that will be discussed later and Fig. 10 includes various amplitudues in the calculations.

Figs. 11 and 12 both show the Regge model predictions for the beam asymmetry and also includes experimental data that is discussed later. However, these figures only show four different values of the kaon center of mass scattering angles.

1.3 Previous Measurements

The differential cross section for $\gamma n \to K^+\Sigma^-$ has been published by the LEPS Collaboration [13] and also by the CLAS Collaboration [14]. LEPS also published the beam asymmetry

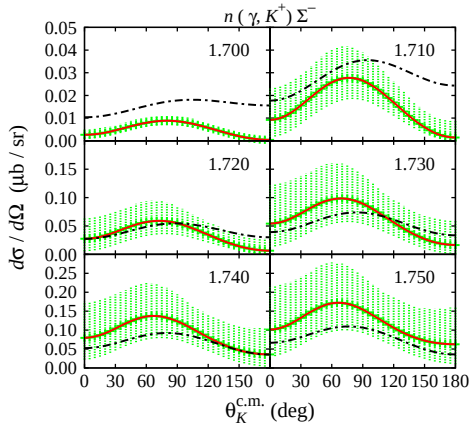

Figure 7: Angular distribution for $\gamma n \to K^+\Sigma^-$ channel. The shaded areas display the uncertainties of Mart's calculations due to the uncertainties in the helicity photon couplings. Figure taken from [9].

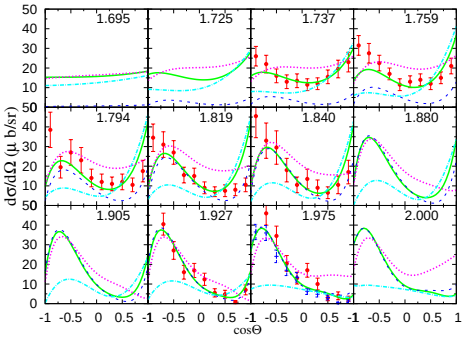

Figure 8: The differential cross section of $\pi^- p \to K^+\Sigma^-$ reaction. The solid (green), dashed (blue), dotted (magenta) and dash-dotted (cyan) lines are the full model calculation, the model calculation with the S11(1650), D15(1675) and F15(1680) turned off, respectively. The numeric values label the center of mass energies in unit of GeV. Figure taken from [11].

Σ [13] for this reaction. Currently, there are no other polarization observable measurements for $\gamma n \to K^+\Sigma^-$ published. The LEPS measurements were only for the forward angle measurements between 0.6 and 1.0 and for photon energies between 1.5 and 2.4 GeV. The beam asymmetry Σ can be seen in Fig. 13. Here, the LEPS measurement shows that the beam asymmetry is close to +1, which indicates the dominance of the K^* exchange in the t-channel.

The CLAS measurements were for a larger angular range between -1.0 and 1.0 and for photon energies between 1.15 and 3.55 GeV. Fig. 14 shows both the LEPS and CLAS measurements together for the differential cross section. LEPS concludes from their measurements, like the beam asymmtry, that the large asymmetries close to +1 indicates the dominance of K^* exchange in the t-channel [13]. They also conclude that the results may imply the existence of a hidden

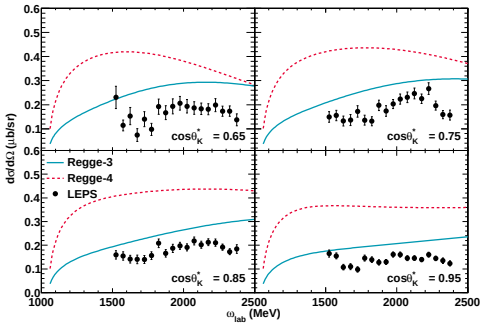

Figure 9: Regge-model predictions for the $n(\gamma, K^+)\Sigma$ differential cross section as a function of the incoming photons lab energy for four different values of the kaon centre-of-mass scattering angle. Data from Ref. [13]. The error bars represent the statistical uncertainties only. The systematic uncertainty is of the order of 20 %. Figure taken from [10].

reaction mechanism and will provide constraints in the model calculations and advance the understanding the $s\bar{s}$ pair production mechanisms [13]. CLAS concludes that at photon energies starting at 1.8 GeV and increasing, a forward peak occurs and is attributed to t-channel mechanisms and is not observed at lower energies, where the dominant contributions appear to be from s-channel mechanisms [14]. Above 2.1 GeV, there are indications of a possible backward peak, which might suggest the presence of u-channel mechanisms [14].

Taking data with deuterium will allow to check the analysis methods and validate them with the existing data just discussed.

2 Experimental Setup

The facility and experimental setup that will be used to collect the data for this proposal will now be described.

2.1 Photon Beam

The A2 photon beam is derived from the production of Bremsstrahlung photons during the passage of the MAMI electron beam through a thin radiator. The resulting photons can be circularly polarized, with the application of a polarized electron beam, or linearly polarized, in the case of a crystalline radiator. The degree of polarization achieved is dependent on the energy of the incident photon beam (E_0) and the energy range of interest, but currently peaks at 75% for linear polarization (see Fig. 15) and 85% for circular polarization (see Fig. 16). The maximum degree of linear polarization is further improved by 5 to 10% by the end of 2009

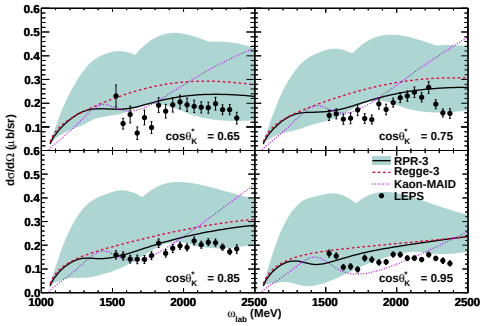

Figure 10: The $n(\gamma, K^+)\Sigma$ differential cross section as a function of the incoming photons lab energy for four different values of the kaon centre-of-mass scattering angle. The dashed curve indicates the Regge-3 model, whereas the full curve corresponds to the RPR-3 amplitude, i.e. Regge-3 supplemented with S11(1650), D33(1700), P11(1710), P13(1720), P13(1900), S31(1900), P31(1910) and P33(1920) resonances. The shaded area takes the uncertainties of the adopted helicity amplitudes into account. These uncertainties are listed in table 1 under SM95. The ratios of EM coupling constants for the P13(1900) resonance are taken in the range [2, 2]. The dotted curve represents the Kaon-MAID [8] predictions. Data from Ref. [13]. Figure taken from [10].

when the collimation and beam monitoring systems will be optimised for MAMI-C during the installation of the Frozen Spin Target. The Glasgow Photon Tagger (see Fig. 16) provides energy tagging of the photons by detecting the post-radiating electrons and can determine the photon energy with a resolution of 2 to 4 MeV depending on the incident beam energy, with a single-counter time resolution $\sigma_t = 0.117$ ns [16]. Each counter can operate reliably to a rate of ≈ 1 MHz, giving a photon flux of $2.5 \cdot 10^5$ photons per MeV. Photons can be tagged in the momentum range from 4.7 to 93.0% of E_0. To augment the standard focal plane detector system and make use of the Tagger's intrinsic energy resolution of 0.4 MeV (FWHM), there exists a

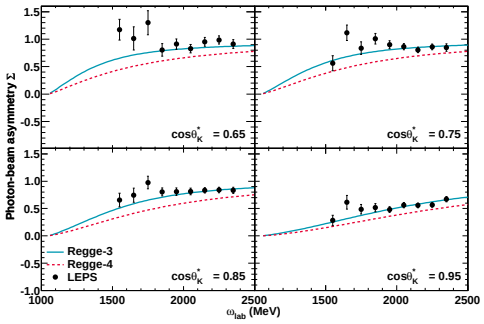

Figure 11: Regge-model predictions for the $n(\gamma, K^+)\Sigma$ photon-beam asymmetry as a function of the incoming photons lab energy for four different values of the kaon centre-of-mass scattering angle. Data from Ref. [13]. The error bars represent the statistical uncertainties only. The systematics are estimated to be $\|\Delta\Sigma\| \approx 0.2$. Figure taken from [10].

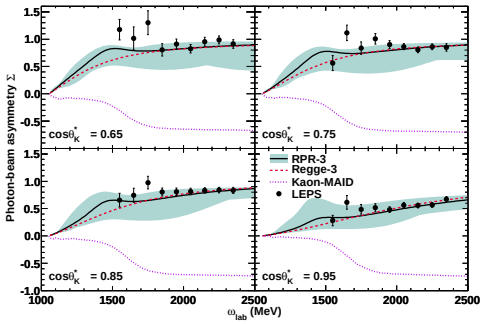

Figure 12: The $n(\gamma, K^+)\Sigma$ photon-beam asymmetry as a function of the incoming photons lab energy for four different values of the kaon centre-of-mass scattering angle. The curves are as indicated in Fig. 10. Data from Ref. [13]. Figure taken from [10].

scintillating fiber detector ('Tagger Microscope') that can improve the energy resolution by a factor of about 6 for a ≈ 100 MeV wide region of the focal plane (dependent on its position) [17].

2.1.1 Upgraded Tagger Focal Plane

The incoming electron energy E_0 is known from the accelerator and the outgoing electron energy E_e from the tagger is known, the photon energy, E_γ can be deduced from the following equation:

$$E_\gamma = E_0 - E_e \ . \tag{1}$$

The current focal plane has 353 plastic scintillators, each 2 cm $\times$ 2 cm $\times$ 8 cm, that are coupled to a photmultiplier tube (PMT). Each scintillator overlaps the neighboring scintillator by $\approx 50\%$. When there is a coincidence between two overlapping scintillators, a hit is recorded in the focal plane, which results in 352 tagger channels. The current focal plane has a maximum electron rate of 10^6. Various rates for different photon energies can be seen in Table 3. Currently, the current tagger setup is in the process of being upgraded to improve the focal plane. The upgrade would consist of replacing the current focal plane with a set of smaller scintillators, each 6 mm $\times$ 6 mm $\times$ 30 mm, coupled to silicon PMTs (SiPMs). This will allow for an increase of the maximum electron rate to $\times 2.5$ with the new readout. By removing the scintillator overlaps from the current design, an additional increase in the maximum electron rate to $\times 2$ is achieved. This allows for a total maximum electron rate of 5×10^6 electrons per tagger channel.

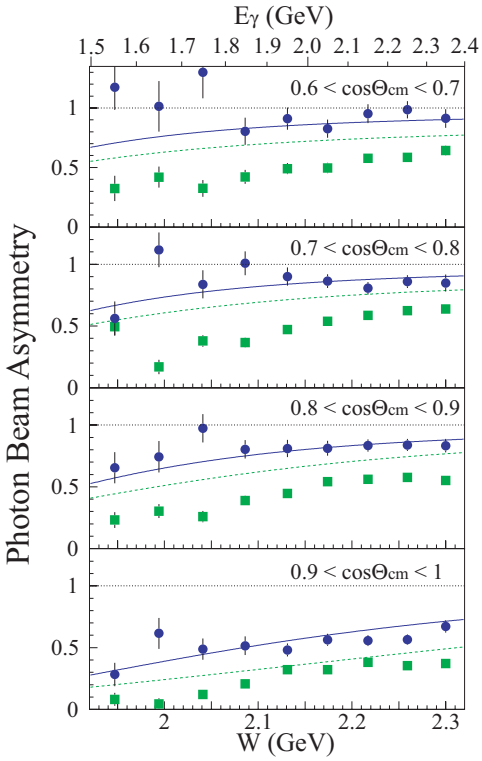

Figure 13: Photon beam asymmetries for $\gamma n \to K^+\Sigma^-$ (circles) and $\gamma p \to K^+\Sigma^0$ (squares). The solid and dashed curves are the Regge model calculations [12, 15] for $K^+\Sigma^-$ and $K^+\Sigma^0$. Figure taken from [13].

2.2 Crystal Ball

The central detector system consists of the Crystal Ball calorimeter combined with a barrel of scintillation counters for particle identification and two coaxial multiwire proportional counters for charged particle tracking. This central system provides position, energy and timing information for both charged and neutral particles in the region between 21° and 159° in the polar angle (θ) and over almost the full azimuthal (ϕ) range. At forward angles, less than 21°, reaction products are detected in the TAPS forward wall. The full, almost hermetic, detector system is shown schematically in Fig. 18 and the measured two-photon invariant mass spectrum is shown in Fig. 19. The Crystal Ball detector (CB) is a highly segmented 672-element NaI(Tl), self triggering photon spectrometer constructed at SLAC in the 1970's. Each element is a truncated triangular pyramid, 41 cm (15.7 radiation lengths) long. The Crystal Ball has an energy resolution of $\Delta E/E = 0.020 \cdot E(GeV)^{0.36}$, angular resolutions of σ_θ = 2-3° and $\sigma_\phi = \sigma_\theta / \sin\theta$ for electromagnetic showers [18]. The readout electronics for the Crystal Ball were completely renewed in 2003, and it now is fully equipped with SADCs which allow for the full sampling of pulse-shape element by element. In normal operation, the onboard summing capacity of these

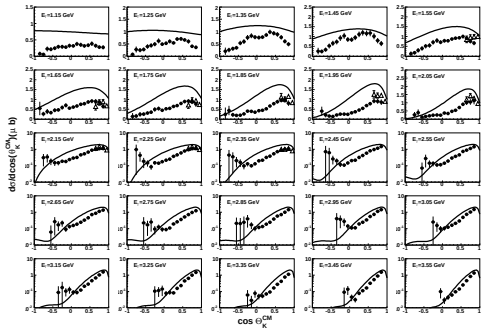

Figure 14: Differential cross sections of the reaction $\gamma d \to K^+\Sigma^-(p)$ obtained by CLAS (full circles). The error bars represent the total (statistical plus systematic) uncertainty. LEPS data [13] (empty triangles) and a Regge-3 model prediction [10] (solid curve) are also shown. Notice the logarithmic scale for high energy plots. Figure taken from [14].

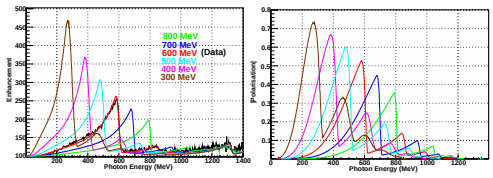

Figure 15: Linear polarization available with the current collimation system for a variety of crystal orientations. The thin black lines are data obtained during recent MAMI-C runs.

ADCs is used to enable dynamic pedestal subtraction and the provision of pedestal, signal and tail values for each element event-by-event. Each CB element is also newly equipped with multi-hit CATCH TDCs. The readout of the CB is effected in such a way as to allow for flexible triggering algorithms. There is an analogue sum of all ADCs, allowing for a total energy trigger, and also an OR of groups of sixteen crystals to allow for a hit-multiplicity second-level trigger, which is ideal for use when searching for high multiplicity final states.

In order to distinguish between neutral and charged particles species detected by the Crystal

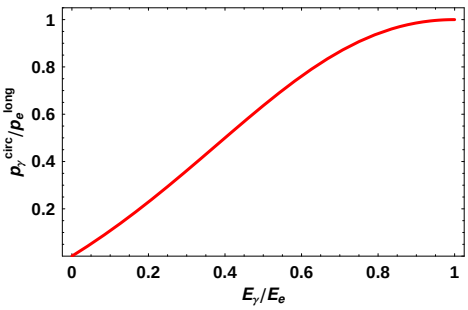

Figure 16: Helicity transfer from the electron to the photon beam as function of the energy transfer. The MAMI beam polarization is $P_e = 85\%$.

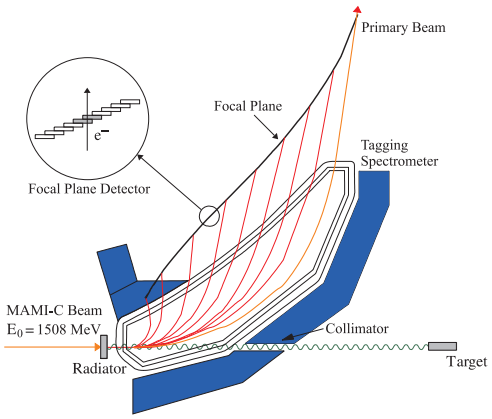

Figure 17: The Glasgow-Edinburgh-Mainz photon tagging spectrometer.

Table 3: Electron rate (s^1) limitations for the current and future focal plane detectors.

	200 MeV	450 MeV	880 MeV	1600 MeV
Current Focal Plane limitations				
Maximum electron rate/per tagger ch.	10^6	10^6	10^6	10^6
Maximum electron rate/per MeV	2×10^6	10^6	0.5×10^6	0.25×10^6
Future Focal Plane limitations				
Maximum electron rate/per tagger ch.	5×10^6	5×10^6	5×10^6	5×10^6
Maximum electron rate/per MeV	10^7	5×10^6	2.5×10^6	1.25×10^6

Ball, the system is equipped with PID2, a barrel detector of twenty-four 50 mm long, 4 mm thick scintillators, arranged so that each PID2 scintillator subtends an angle of 15° in ϕ. By matching a hit in the PID2 with a corresponding hit in the CB, it is possible to use the locus of the ΔE, E combination to identify the particle species (see Fig. 20). This is primarily used for the separation of charged pions, electrons and protons. The PID2 covers from 15° to 159° in θ. The excellent CB position resolution for photons stems from the fact that a given photon triggers several crystals and the energy-weighted mean of their positions locates the photon position to better than the crystal pitch. For charged particles which deposit their energy over only one or two crystals, this is not so precise. Here the tracks of charged particles emitted within the angular and momentum acceptance of the CB detector will be reconstructed from the coordinates of point of intersections of the tracks with two coaxial cylindrical multiwire proportional chambers (MWPCs) with cathode strip readout. These MWPCs are similar to

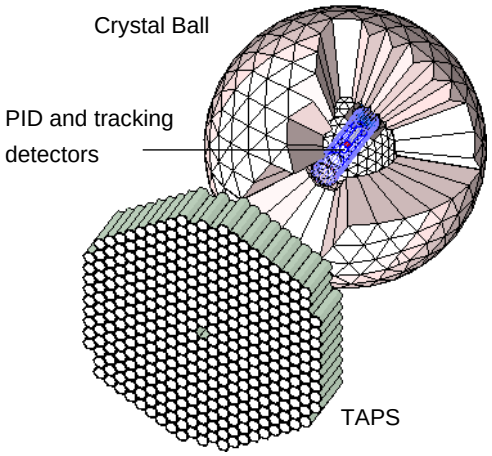

Figure 18: The A2 detector setup: the Crystal Ball calorimeter with cut-away section showing the inner detectors and the TAPS forward wall.

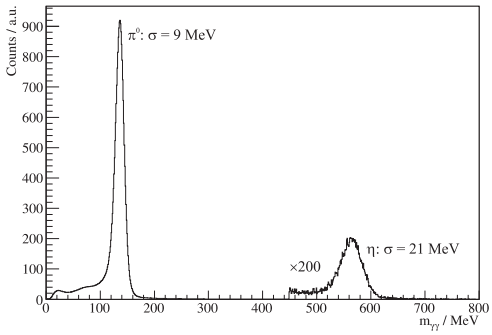

Figure 19: Two γ invariant mass spectrum for the CB TAPS detector setup. Both η and π^0 mesons can be clearly seen.

those installed inside the CB during the firrst round of MAMI-B runs [19]. The most significant difference is that all detector signals are taken at the upstream end of the MWPCs, minimising the material required and facilitating particle detection in the forward polar region. A mixture of argon (79.5%), ethane (30%) and freon-CF4 (0.5%) is used as the filling gas. This mixture is a compromise between charge multiplication and localization requirements imposed by the ionizing particle tracks. Within each chamber both the azimuthal and the longitudinal coordinates of the avalanche will be evaluated from the centroid of the charge distribution induced on the cathode strips. The location of the hit wires(s) will be used to resolve ambiguities which arise from the fact that each pair of inner and outer strip cross each other twice. The expected angular resolution (rms) will be $\approx 2^\circ$ in the polar emission angle θ and $\approx 3^\circ$ in the azimuthal emission angle ϕ. The MWPCs have been recently installed inside the CB frame and their calibration using both cosmic rays and test beam data is currently underway.

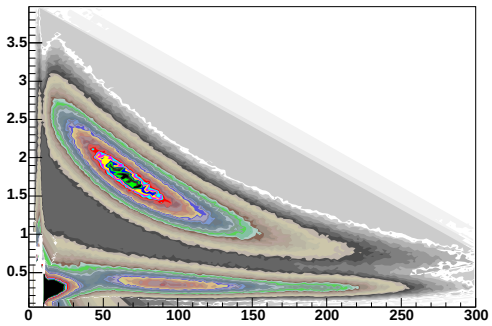

Figure 20: A typical ΔE versus E plot from the PID detector. The upper curved region is the proton locus, the lower region contains the pions and the peak towards the origin contains mostly electrons.

2.3 TAPS

The TAPS forward wall is composed of 384 BaF_2 elements, each 25 cm in length (12 radiation lengths) and hexagonal in cross section, with a diameter of 59 mm. The front of every TAPS element is covered by a 5 mm thick plastic veto scintillator. The single counter time resolution is $\sigma_t = 0.2$ ns, the energy resolution can be described by $\Delta E/E = 0.018 + 0.008/E(GeV)^{0.5}$ [20]. The angular resolution in the polar angle is better than 1°, and in the azimuthal angle it improves with increasing θ, being always better than 1/R radian, where R is the distance in centimeters from the central point of the TAPS wall surface to the point on the surface where the particle trajectory meets the detector. The TAPS readout was custom built for the beginning of the CB@MAMI program and is effected in such a way as to allow particle identification by Pulse Shape Analysis (PSA), Time Of Flight (TOF) and ΔE/E methods (using the energy deposit in the plastic scintillator to give ΔE). TAPS can also contribute to the CB multiplicity trigger and is currrently divided into upto six sectors for this purpose. The 2 inner rings of 18 BaF_2 elements have been replaced recently by 72 $PbWO_4$ crystals each 20 cm in length (22 radiation lengths). The higher granularity improves the rate capability as well as the angular resolution. The crystals are operated at room temperature. The energy resolution for photons is similar to BaF_2 under these conditions [21].

2.4 Targets

Two targets are desired to achieve full potential of the proposed measurements. A third target of carbon is only desired for background subtraction.

2.4.1 Liquid Deuterium

The A2 liquid deuterium (LD_2) target cell is made from Kapton and is 125 μm thick, roughly 3 cm long, and has a diameter of 4 cm. Gaseous deuterium is kept in a storage tank at typically 1400 mbar at the beginning of the cooling. To liquify the deuterium, the target will be cooled down to approximately 20 K and wrapped in an isolating foil made from 8 μm of Mylar and 2 μm of aluminum. About 25% of the deuterium is liquified and the pressure in the gas drops to 1080 mbar. The liquid deuterium is led to a storage reservoir and finally to the target cell. The temperature in the target cell is monitored and adjusted automatically by either adding cool liquid or heating. Inside the tube, there is a vacuum of around $3 \cdot 10^7$ mbar. More target information can be seen in Table 4.

Table 4: Various target parameters of the different targets in A2. L_t refers to the target length, ρ_t refers to the target density, M_{mol} is the molar mass, and N_t refers to surface density of the target.

target material	L_t (cm)	ρ_t (g/cm^3)	M_{mol} (g/mol)	N_t (b^{-1}
LD_2	3.02	0.16324	2.014	0.14741
C_4D_9OD	2	1.1	84.1923	0.09442
Carbon	1.98	0.57	12.011	0.05659

2.4.2 Frozen Spin Target

Polarization experiments using high density solid-state targets in combination with tagged photon beams can reach the highest luminosities. For the double polarization measurements planned with the Crystal Ball detector on polarized protons and deuterons, a specifically designed, large horizontal ^{3}He/^{4}He dilution refrigerator was built in cooperation with the Joint Institute for Nuclear Research (JINR), Dubna (see Fig. 21). It has minimum limitations for the particle detection and fits into the central core of the inner Particle Identification Detector (PID2). This was achieved by using the frozen spin technique with the new concept of placing a thin superconducting holding coil inside the polarization refrigerator. Large longitundinal and transverse polarizations can be achieved.

Highest nucleon polarization in solid-state target materials is obtained by a microwave pumping process, known as 'Dynamic Nucleon Polarization' (DNP). This process is applicable to any nucleus with spin and has already been used in different experiments with polarized proton

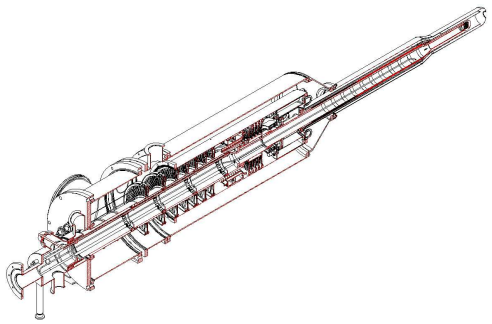

Figure 21: The new dilution refrigerator for the Crystal Ball detector.

and deuteron targets. The geometric configuration of the target is the same for the polarized proton and neutron setup. However, since the polarization measurement of the deuteron is more delicate due to the small size of the polarization signals, the modification of some basic components is needed. The reason for this is twofold: firstly, the magnetic moment of the deuteron is smaller than that of the proton and, in addition, the interaction of the deuteron quadrople moment with the electric field gradient in the sample broadens the deuteron polarization signal. An accuracy $\Delta P_p/P_p$ of 2 to 3% for the protons and $\Delta P_D/P_D$ of 4 to 5 % for the deuterons is expected in the polarization measurement. It has also to be taken into account that the measured deuteron polarization P_D is not equal to the neutron polarization P_n. Assuming a 6% admixture of the D-state of the deuteron, a calculation based on the Clebsch-Gordon coefficients leads to $P_n = 0.91 P_D$. Several polarized proton and deuteron materials are available such as alcohols and deuterated alcohols (e.g. butanol C_4H_9OH), NH_3, ND_3, or ^{6}LiD. The most important criteria in the choice of material suitable for particle physics experiments are the degree of polarization P and the ratio k of free polarizable nucleons to the total number of nucleons. Further requirements on polarized target materials are a short polarization build-up time and a simple, reproducible target preparation. The polarization resistance against radiation damage is not an issue for experiments with a low intensity tagged photon beam ($N^{\cdot} \approx 5 \cdot 10^7 s^{-1}$) as will be used here. However, the limitations of a reduced relaxation time due to overheating of the target beads (Kapitza resistance) will have to be investigated.

Taking all properties together, butanol and deuterated butanol are the best material for this experiment. For protons, a maximum polarization of $P_p = 90\%$ is expected and an average polarization of $P_p = 70\%$ in the frozen spin mode. Recently, a deuteron polarization of $P_D = 80\%$ was obtained with Trityl doped butanol targets at 2.5 T magnetic field in a ^{3}He/^{4}He dilution refrigerator. At a 0.4 T holding field, an average neutron polarization P_n of 50% will be obtained.

The filling factor for the ≈ 2 mm diameter butanol spheres into the 2 cm long, 2 cm diameter target container will be around 60%. The experience from the GDH runs in 1998 [22] shows that with a total tagged photon flux of $5 \cdot 10^7$, relaxation times of about 200 hours can be expected. More target information can be seen in Table 4.

In conclusion, it is estimated that the following target parameters will be achieved:

- Maximum total tagged photon flux in the energy range of 4.7 to 93% of E_o: $N*_\gamma \approx 5 \cdot 10^7 s^{-1}$, with relaxation time of 200 hours.
- Target proton density in 2 cm cell: $N_T \approx 9.1 \cdot 10^{22} cm^{-2}$ (including dilution and filling factors).
- Average proton polarization $P_p = 70\%$.
- Target deuteron density in 2 cm cell: $N_T \approx 9.4 \cdot 10^{22} cm^{-2}$ (including dilution and filling factors).
- Average neutron polarization $P_n = 50\%$.

2.4.3 Carbon

To understand the unpolarised background contributions inside dButanol, additional measurements with a carbon foam target will be required. The density of the carbon target should be chosen in such a way that the number of carbon nuclei matches the number of carbon nuclei inside the dButanol material. The carbon foam target should have a density of ≈ 0.57 g/cm^3. To create similar experimental conditions as for the dButanol target, the carbon foam target should also be placed inside the cryostat and cooled down as well.More target information can be seen in Table 4.

3 Beamtime Conditions

Various beamtime conditions will be discussed now such as how to access the kaon, the trigger, beamtime estimates, and the photon flux.

3.1 Accessing the Kaon

Typically, A2 is not well-known for performing measurements on reactions of kaons. However, in [23], it was shown that the K^+ can be accessed through it's two dominant decay modes, which

are $K^+ \rightarrow \mu + \nu\mu$ (muonic) and $K^+ \rightarrow \pi + \pi^0$ (pionic), with branching ratios of 64% and 21%, respectively.

The analysis from [23] will now be described. Each cluster of hit crystals produced from a charged particle event in the Crystal Ball was separated into two sub-clusters. The incident-cluster (IC) comprised those crystals having a timing coincidence within $\pm 3\sigma$ of the timing of the reaction in the target, where σ is the achievable coincidence timing resolution ($\approx$3 ns). Only events with a summed IC energy above 25 MeV and consisting of only one or two crystals were retained. The crystals with coincidence times at least 10 ns later than the photoreaction were assumed part of the decay-cluster (DC) from the decay of the stopped K^+. A minimum summed DC energy of 75 MeV and at least 4 crystals in the DC was required. To separate events into the two dominant K^+ decay modes, two parameters were used: the fractional energy in the furthest crystal in the DC with respect to the total energy in the DC (the decay energy localization) and the average difference in angle between each crystal in the DC and the IC (the decay cluster linearity). In the analysis of [23], only events from the dominant muonic decay of K^+ were retained for further analysis.

The IC summed energy was then utilized in a ΔE versus E analysis with the ΔE provided by the signal in the PID and used to reconstruct the momentum of the K^+. This new K^+ identification technique enables K^+ detection without the need for large scale spectrometers or Cerenkov detectors.

However, this analysis technique by [23] can only be applied to well identified double cluster configurations. Therefore, the author is applying for funding to build an aerogel detector specifically designed for detecting charged kaons in A2.

Using Geant4, a rendering has been made to show that an aerogel detector can easily be accomodated in the Crystal Ball/TAPS experiment. Figs. 22 and 23 show the overview. This detector will allow for distinguishing between charged particles such as kaons and charged pions. At higher energies, there is more chances of misidentification when no spectrometer magnet is present. Therefore, not every reaction has to be investigated, but a few choice reactions have final state particles that can be easily detected in the aerogel.

An active aerogel area with a height of roughly 100 cm and a width of roughly 65 cm is proposed. The aerogel detector will consist of layers of aerogel in a light diffusing reflection box. The light generated will be collected by PMTs. To allow for K^+/p separation, aerogels with more than one index of refraction is required. A hit is detected when the particle is faster than the speed of light in that particular medium. By choosing the appropriate index of refraction

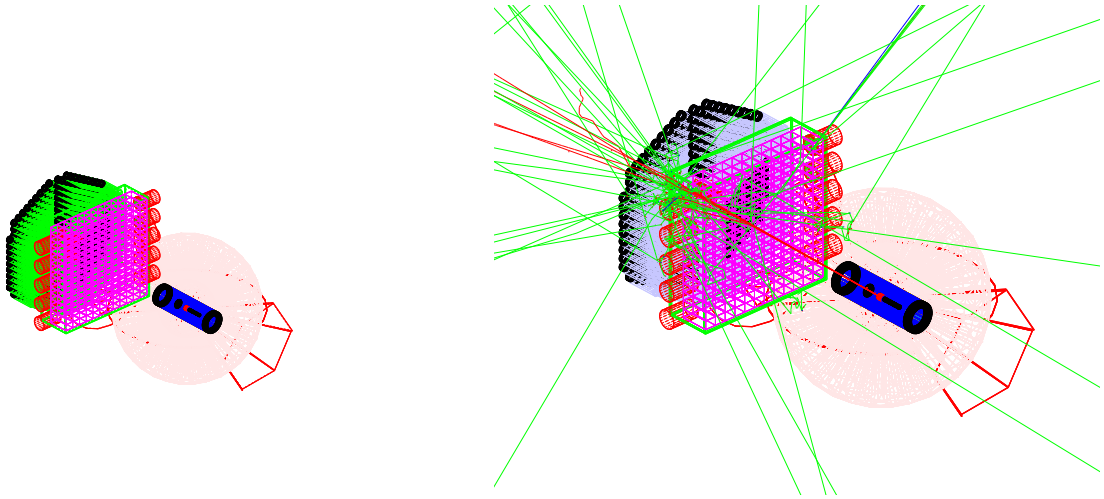

Figure 22: Rendering of the aerogel detector used in conjunction with the Crystal Ball/TAPS experiment.

for one layer of aerogel, the following equation follows:

$$c_{medium} = \frac{c}{n_{index}} \ ,$$

where c_{medium} is the speed of the particle in the medium, c is the speed of light, and n_{index} is refractive index, and this will allow the pion or kaon to fall between the β versus momentum lines of the particles. A second layer of aerogel with a different refractive index can give signals for pions and kaons, but not for protons.

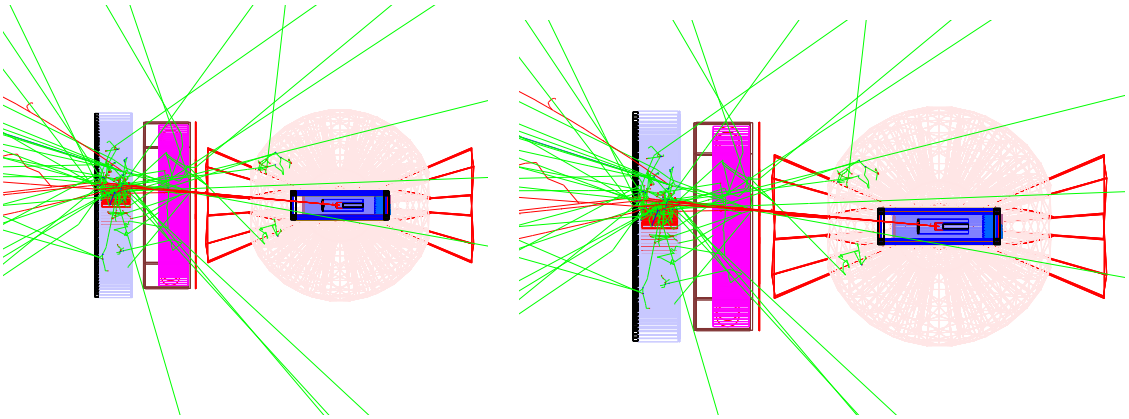

Figure 23: Rendering of the aerogel detector used in conjunction with the Crystal Ball/TAPS experiment.

The building of an aerogel detector to be used in A2 at MAMI can assist in understanding the hadron structure by means of quarks and the gluonic degrees of freedom. By securing funds to build the detector, it is clear that data can be acquired to assist in contributing significantly to directly accessing the charged kaon particle detection.

3.2 Trigger

The data acquisition of A2 was upgraded in 2013. Because of the long rise-time of the signal from the NaI(Tl) crystals of the CB, the trigger is divided into a Level-1 and a Level-2 trigger. The Level-1 trigger is based on the total energy deposited in the CB. The analog sum of all the CB signals is built and discriminated by a Leading Edge Discriminator (LED), which leads to different trigger times when the signals have different amplitudes, referred to as time walk. For the experiment, the CB energy sum threshold should be set to approximately 300 MeV to reject events from single pion production. Thus, only events with more than 300 MeV deposited energy in the CB will be recorded. In addition to the CB energy sum, a multiplicity trigger can contribute to the Level-2 trigger. Each crystal in the CB is assigned to a group of 16 adjacent channels and when at least one of these crystals registers an energy above a certain threshold, the group adds to the total multiplicity. In both the CB and TAPS, the energy of at least one crystal of a segment has to be larger than the LED1 threshold to contribute to the total multiplicity. A M2+ trigger is a trigger which requires at least a multiplicity of two in the combined setup of the CB and TAPS.

3.3 Photon Flux

To allow for proper normalization of cross sections or observable measurements, the flux of the incident photons on the target is required. The photon flux, N_γ, is given by the number of electrons in the tagger, N_{e^-} multiplied with the tagging efficiency ϵ_{tagg} and the average electron rate, a:

$$N_\gamma = N_{e-} \cdot \epsilon_{tagg} \cdot a \ . \tag{2}$$

The collimation of the beam and the beam quality and position directly influence the tagging efficiency measurements. As previously discussed, due to the upcoming upgrade to the tagger, a maximum electron rate is given as $N_{e^-} = 1.25 \cdot 10^6$ electrons $MeV^{-1}s^{-1}$. The average electron rate, a is roughly 60% of N_{e^-}, which is $7.5 \cdot 10^5$. Previous tagging efficiencies in A2 are given in Table 5. Based on the numbers given in Table 5, one can estimate that when using a 2 mm collimator, a tagging efficiency ϵ_{tagg} of $\approx 30\%$ can be achieved. This would then give a maximum photon flux, N_γ, as $2.8 \cdot 10^{11}$.

Table 5: Tagging Efficiency Values

E_e (MeV)	Collimator (mm)	Efficiency %
450	1.5 (active target)	3.8
450	2.5	8.3
883	2	18.0
1557	1.5 (dButanol)	20.9
1557	2 (dButanol)	30.1
1557	2.5 (C target)	37.6
1557	2.5 (Pb target)	35.1
1557	2.5 (Al target)	31.9
1557	3	48.8

3.4 Beamtime Estimate

The necessary beam time is given by:

$$\Delta t = [\delta^2_{stat} \cdot \Delta\sigma_0 \cdot N_\gamma \cdot N_t \cdot \epsilon \cdot b_K]^{-1} \ , \tag{3}$$

where:

- δ^2_{stat}: relative statistical uncertainty
- $\Delta\sigma_0$: unpolarized cross section in the respective energy bins
- N_γ: number of photons per 20 MeV incident photon energy
- N_t: surface density of target nuclei
- ϵ: detection efficiency, calculated from MC simulation
- b_K: decay branching ratio of $\Sigma^- \to \pi^- n = 99.85\%$

Here, δ^2_{stat} is $\approx 10\%$. $\Delta\sigma_0$ is ≈ 0.2 microbarns. N_γ, calculated previously, is $2.8 \cdot 10^{11}$. For LD_2, N_t is 0.14741, for C_4D_9OD, N_t is 0.09442, and for carbon, N_t is 0.05659. ϵ was calculated to be ≈ 0.5. Finally, b_K, known from [6], is 99.85%.

With these numbers, a beam time estimate for liquid deuterium is 200 hours and for polarized deuterated butanol is 500 hours. An additional 100 hours is requested of running with a carbon target for background subtraction. Therefore, the total beamtime request is 800 hours.

References

[1] S. Capstick and W. Roberts, Phys. Rev. D**47**, 1994 (1993).

[2] S. Capstick and W. Roberts, Phys. Rev. D**49**, 4570 (1994).

[3] S. Capstick and W. Roberts, Phys. Rev. D**58**, 074011 (1998).

[4] W.-T. Chiang and F. Tabakin, Phys. Rev. C**55**, 2054 (1997).

[5] G. Knöchlein, D. Drechsel, and L Tiator, Z. Phys. A**A352**, 327 (1995).

[6] K. A. Olive *et al.* (Particle Data Group), Chin. Phys. C**38**, 090001 (2014).

[7] J.-M. Laget, Phys. Rep. 69, 1 (1981); Phys. Lett. B 259, 24 (1991); nucl-th/0507035 (2005).

[8] T. Mart, C. Bennhold, H. Haberzettl, and L. Tiator, Kaon-MAID available from `http://www.kph.uni-mainz.de/MAID/kaon/kaonmaid.html`.

[9] T. Mart, Phys. Rev. C**90**, 065202 (2014).

[10] P. Vancraeyveld, L. De Cruz, J. Ryckebusch and T. Van Cauteren, Phys. Rev. C**73**, 045207 (2006).

[11] Xu Cao, V. Shklyar, and H. Lenske, Phys. Rev. C**88**, 055204 (2013).

[12] M. Guidal *et al.*, Nucl. Phys. **A627**, 645 (1997).

[13] H. Kohri *et al.*, Phys. Rev. Lett. **97**, 082003 (2006).

[14] S. Anefalos Pereira *et al.*, Phys. Rev. Lett. **B688**, 289 (2010).

[15] T. Mart and C. Bennhold, nucl-th/0412097.

[16] J. C. McGeorge *et al.*, Eur. Phys. J. **A** (2008).

[17] A. Reiter *et al.*, Eur. Phys. J. **A** (2006).

[18] S. Prakhov *et al.*, Phys. Rev. C**79**, 035204 (2009).

[19] G. Audit *et al.*, Nucl. Instr. Meth. **A** 301 473 (1991).

[20] S. Prakhov *et al.*, Phys. Rev. C**79** 035204 (2009).

[21] R. Novotny *et al.*, Nucl. Instr. Meth. **A** 486 131 (2002).

[22] A. Thomas *et al.*, Nucl. Phys. **B79**, 591 (1999).

[23] T.C. Jude *et al.*, Phys. Rev. Lett. **B735**, 112 (2014).